Journal of Power Sources 196 (2011) 3195–3203

Contents lists available at ScienceDirect

Journal of Power Sources

journal homepage: www.elsevier.com/locate/jpowsour

Pore scale modeling of a proton exchange membrane fuel cell catalyst layer: Effects of water vapor and temperature

Kyle J. Lange[a,*], Pang-Chieh Sui[a], Ned Djilali[b]

[a] Institute for Integrated Energy Systems, University of Victoria, BC, Canada
[b] Institute for Integrated Energy Systems and Department of Mechanical Engineering, University of Victoria, BC, Canada

ARTICLE INFO

Article history:
Received 7 October 2010
Received in revised form
18 November 2010
Accepted 22 November 2010
Available online 2 December 2010

Keywords:
PEM fuel cell
Catalyst layer
Effective transport properties pore scale model
Effective thermal conductivity

ABSTRACT

A pore scale model of a polymer electrolyte membrane (PEM) fuel cell cathode catalyst layer is developed which accounts for species transport, electrochemical reactions and thermal transport. Effective transport parameters are computed over a range of operating conditions including the effective oxygen diffusivity, effective water vapor diffusivity, effective proton conductivity, effective electron conductivity and the effective thermal conductivity. In addition, the total amount of oxygen consumption is computed for different operating conditions. Finally, a critical assessment of the impact of assumptions made in the absence of detailed morphological data is presented.

1. Introduction

Catalyst layers are at the heart of PEM fuel cells. They provide pathways for the transport of reactants, protons, electrons and producs while facilitating oxygen reduction at the cathode and hydrogen oxidation at the anode. Catalyst layers are composed of four phases: carbon, which allows for conduction of electrons and support the platinum nanoparticles; ionomer binding, which provides a path for proton conduction; platinum nanoparticles, which provide sites for electrochemical reactions; and pores, which allow reactant and product gases to diffuse through the catalyst layer. All of these phases are present in an extremely thin layer (of the order of 10 μm), which is bounded on one side by the gas diffusion layer or microporous layer and on the other side by the polymer electrolyte membrane.

The primary issues which prevent the commercialization of PEM fuel cells are high cost, degradation and poor cell performance. The high cost is related to the amount of platinum that is used in catalyst layers. Improving the utilization of the platinum particles in catalyst layers, particularly on the cathode side, has the potential to substantially reduce the cost of PEM fuel cells [1]. Degradation of the ionomer, carbon supports and platinum particles is also a significant issue [2,3]. Understanding the mechanisms by which these degradations occur can lead to mitigation strategies that can improve the operating lifetime of fuel cells. Finally, the poor cell performance that is experienced by PEM fuel cells is due to a large activation polarization and mass-transport losses at the cathode. The activation polarization is caused by sluggish kinetics of the oxygen reduction reaction, and is particularly large because of the low operating temperature of PEM fuel cells. The most severe mass transport losses are caused by the accumulation of liquid water at reaction sites, which is often referred to as "flooding". Additionally, significant ohmic losses through the membrane can occur at dry conditions [4].

Because the catalyst layer is so thin, it is very difficult to do experimental studies which could provide information that would allow one to reduce the cost and degradation or improve the performance of a PEM fuel cell. Because of this, there has been a surge of interest in computational simulation and reconstruction of the catalyst layer at the mesoscale level. It is hoped that simulations will eventually provide a cost-effective approach for designing optimum catalyst layer microstructures. However, there are still substantial gaps in the existing body of knowledge that prevent current simulation tools from having these predictive capabilities. Nonetheless, mesoscale simulations can provide valuable information such as the effective transport properties through the catalyst layer. These properties could be provided to a macroscale model as part of a multiscale fuel cell model. In addition, important ideas about multiphase transport through nanoscale porous media could be obtained from these models.

* Corresponding author. Tel.: +1 250 721 8935; fax: +1 250 721 6323.
E-mail address: klange@uvic.ca (K.J. Lange).

0378-7753/$ – see front matter © 2010 Elsevier B.V. All rights reserved.
doi:10.1016/j.jpowsour.2010.11.118

The first published work on catalyst layer simulations was done by Wang [5] in two dimensions. This model, which included proton transport, oxygen transport and electrochemical reactions, was later extended to three dimensions and applied to a regular microstructure [6] and a random microstructure [7]. In the three-dimensional models, electron transport was neglected because ion transport was assumed to be the limiting factor for the oxygen reduction reaction. The production and transport of water was also accounted for in the three-dimensional model. Additional simulations were done on a catalyst layer structure that was reconstructed to match a physical catalyst layer using stochastic methods [8]. This work was further extended to identify an optimum design [9], based on a series of parametric studies rather than multi-parameter numerical optimization [10,1]. These simulations modeled the entire length of the catalyst layer and had a resolution of 250 nm.

Kim and Pitsch [11] used a different approach to catalyst layer reconstruction and simulation. They represented the catalyst layer as consisting of carbon spheres surrounded by an ionomer film. The catalyst layer reconstruction was done using a simulated annealing technique, where the spheres were randomly moved in order to obtain a prescribed porosity and two-point autocorrelation function. The catalyst layer was modeled with a resolution of 8 nm and a $1\,\mu m \times 1\,\mu m \times 1\,\mu m$ section was considered. They used a Lattice–Boltzmann method to simulate the transport of oxygen and protons through the catalyst layer, but their simulation did not account for electrochemical reactions. Knudsen diffusion was accounted for by computing an average pore radius which was used to compute a Knudsen diffusion coefficient for all pores in the solution domain. They obtained effective transport parameters for oxygen and protons, and expressed the relationship between volume fractions and effective transport parameters by using a power law approximation.

More recently, a small section of a PEM fuel cell catalyst layer was reconstructed and modeled at a resolution of 2 nm [12]. A random reconstruction algorithm which attempted to account for agglomeration was considered in the model. In addition, a different Knudsen number was used for each pore cell based on the diameters in the *x*-, *y*- and *z*-directions. Effective transport properties for oxygen diffusivity and proton conductivity were computed for five different geometries. Specific attention was focused on the number of seeds available for agglomerates to grow on.

In a previous paper [13], the authors used a stochastic approach to reconstruct a section of a PEM fuel cell catalyst layer and modeled oxygen diffusion, proton conduction, electron conduction and electrochemical reactions for a wide range of random microstructures. Hundreds of different microstructures were used, resulting in a large number of effective transport parameters at different pore, ionomer and carbon volume fractions. The microstructural parameters for the reconstructed catalyst layer were changed to determine how this would affect effective transport parameters and total consumption values. One of the key findings of this work was that when larger carbon spheres are used in the catalyst layer, higher effective oxygen diffusivities and proton conductivities are obtained.

The current work builds on the previous work [13] and extends the model to account for water vapor concentration and temperature. The effects of water vapor diffusion, electro-osmotic drag, thermal conduction, ohmic heating, and activation losses are considered. The fully coupled set of discretized governing equations is solved for a wide range of microstructures at various temperatures, oxygen concentrations, and water vapor concentrations. Effective oxygen diffusivities, effective water vapor diffusivities, effective proton conductivities and effective electron conductivities are computed for a wide range of microstructures. In addition, effective thermal conductivities for different microstructures are computed. To the knowledge of the authors, this is the first mesoscale PEM fuel cell catalyst layer simulation to obtain effective thermal conductivity data.

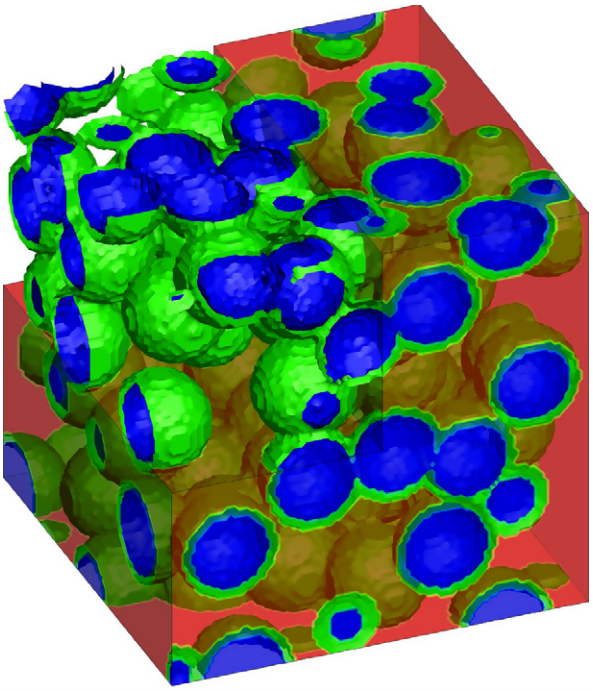

Fig. 1. Typical stochastically reconstructed catalyst layer section ($200\,nm \times 200\,nm \times 200\,nm$). Carbon spheres are in blue, ionomer is green, and pores are orange and red.

2. Numerical method

2.1. Catalyst layer reconstruction

A stochastic method is used to reconstruct random microstructures which represent pieces of the catalyst layer. Carbon spheres are randomly placed in the domain subject to several constraints. Each carbon sphere has a probability that it will be required to overlap with a previously placed sphere, but it can only overlap by an amount that is less than the specified overlap tolerance. Once all the carbon spheres have been placed in the domain, an ionomer layer of a given thickness is extruded from the sphere surfaces. Thus the domain consists of three phases: carbon, ionomer, and pores. More details of the reconstruction algorithm have been given in previous works [14,13] and are not repeated here. In the current work, an ionomer thickness of 4 nm is used along with carbon sphere radii of 12 nm and 20 nm. An overlap probability of 0.9 is used (representing the tendency of carbon particles to agglomerate) and an overlap tolerance of 0.01 is used (rigid carbon spheres will not have a significant overlap). The domain size considered in this work is $200\,nm \times 200\,nm \times 200\,nm$, which is discretized with a $100 \times 100 \times 100$ structured mesh. The stochastic simulations performed in this study required the generation of hundreds of different computational samples; an example is shown in Fig. 1.

2.2. Governing equations

The model incorporates governing equations for oxygen, water vapor, protons, electrons, and temperature. Steady-state operating conditions are assumed and gas transport is assumed to take place through binary diffusion. The effects of liquid water are not considered in the model. The electrochemical reactions are assumed to take place uniformly at the carbon/ionomer interface and the

Tafel approximation is used, which is valid at the cathode for high current densities.

The continuity equation for oxygen is composed of two expressions which represent diffusion and consumption through electrochemical reactions, and is given as

$$\nabla \cdot \left(-D_{O_2} \nabla c_{O_2} + 1_{int} \left[\frac{1}{4F} i_0 \frac{c_{O_2}}{c_{O_2,ref}} \exp\left(\frac{-\alpha_c F}{RT} \eta \right) \right] \right) = 0, \quad (1)$$

where c_{O_2} is the oxygen concentration, F is Faraday's constant, $c_{O_2,ref}$ is the oxygen concentration at standard temperature and pressure, R is the universal gas constant and T is the temperature. The first part of Eq. (1) represents oxygen diffusion. Because of the small pore diameters in the catalyst layer, Knudsen diffusion must be accounted for in the pore regions. The Knudsen diffusivity for oxygen is computed according to the dusty gas model [15,16] as [17–19]

$$D_{O_2,Kn}\,(\mathrm{cm^2\,s^{-1}}) = 4850 d_p \sqrt{\frac{T}{32}}, \quad (2)$$

where d_p is the local pore diameter for a given pore cell, which is computed by taking an average of 13 different lengths as described in a previous work [13]. The bulk diffusivity is given according to binary diffusion of oxygen into nitrogen [20] as

$$D_{O_2,b}\,(\mathrm{cm^2\,s^{-1}}) = 2.2 \times 10^{-1} \frac{(T/(293.2\,\mathrm{K}))^{3/2}}{p/(1\,\mathrm{atm})}, \quad (3)$$

where p is the pressure of the catalyst layer, which is taken to be 2 atm in the current work. The total oxygen diffusivity in the pore region is computed using the Bosanquet approximation [21] as

$$\frac{1}{D_{O_2}} = \frac{1}{D_{O_2,Kn}} + \frac{1}{D_{O_2,b}}. \quad (4)$$

The carbon phase is assumed to be impermeable to oxygen, but the oxygen diffusivity through Nafion which has been recast at a temperature of 120 °C is taken from experimental data [22] to be

$$D_{O_2,i}\,(\mathrm{cm^2\,s^{-1}}) = 10^{-6} \times (0.1543(T - 273) - 1.65). \quad (5)$$

The second part of Eq. (1) refers to the consumption of oxygen through electrochemical reactions. The term 1_{int} is included to denote that this term is only nonzero at the interfaces of carbon and ionomer cells. In this respect, the model considers an idealized scenario where a very thin platinum layer uniformly covers the carbon spheres and the electrochemical reaction takes place at every carbon/ionomer interface. As the model is further developed, discrete platinum particles will be considered along with a correlation between the platinum loading and the number of platinum particles. The exchange current density i_0 and the cathodic charge transfer coefficient α_c are given according to experimental data from a platinum/Nafion electrode [23] as

$$i_0\,(\mathrm{A\,cm^{-2}}) = (0.029825) 10^{-1521.93/T}, \quad (6)$$

$$\alpha_c = (2.25 \times 10^{-3}) T - 1.78 \times 10^{-1}. \quad (7)$$

The overpotential is given as

$$\eta = \phi_s - \phi_m, \quad (8)$$

where ϕ_s is the solid potential and ϕ_m is the membrane potential.

The governing equation for water vapor includes terms for diffusion, electro-osmotic drag, and production through electrochemical reactions. It is given as

$$\nabla \cdot \left(-D_{H_2O} \nabla c_{H_2O} - \frac{n_d \sigma_m}{F} \nabla \phi_m - 1_{int} \times \left[\frac{1}{2F} i_0 \frac{c_{O_2}}{c_{O_2,ref}} \exp\left(\frac{-\alpha_c F}{RT} \eta \right) \right] \right) = 0, \quad (9)$$

Table 1
Curve-fit coefficients and parameter values used in the simulation.

Coefficient	Value	Coefficient	Value
c_1	2.8133×10^{-4}	p_1	−2846.4
c_2	1.328355	p_2	−411.24
c_3	-1.1642×10^{-2}	p_3	−10.554
c_4	3.442175×10^{-5}	p_4	0.16636
c_5	-3.33815×10^{-8}		
c_6	-7.2939×10^{-4}		

where c_{H_2O} is the water vapor concentration, n_d is the electro-osmotic drag coefficient, and σ_m is the membrane conductivity. In the pore region, the expressions for the Knudsen diffusivity of water vapor [17–19] and the bulk diffusivity of water vapor [20] are given as:

$$D_{H_2O,Kn}\,(\mathrm{cm^2\,s^{-1}}) = 4850 d_p \sqrt{\frac{T}{18}}, \quad (10)$$

$$D_{H_2O,b}\,(\mathrm{cm^2\,s^{-1}}) = 2.93 \times 10^{-1} \frac{(T/298.2\,\mathrm{K})^{3/2}}{p/(1\,\mathrm{atm})}. \quad (11)$$

The Bosanquet approximation [21] is used to compute the total water vapor diffusivity in the pore region as

$$\frac{1}{D_{H_2O}} = \frac{1}{D_{H_2O,Kn}} + \frac{1}{D_{H_2O,b}}. \quad (12)$$

For the ionomer region, the water vapor diffusivity is given as [24]

$$D_{H_2O,i}\,(\mathrm{cm^2\,s^{-1}}) = 6.0 \times 10^{-6}. \quad (13)$$

The water vapor diffusivity in the carbon region is set to zero. The value for the electro-osmotic drag coefficient n_d is taken to be 1 [25].

The proton continuity equation consists of two terms which represent proton conduction and consumption of protons through electrochemical reactions. It is given as

$$\nabla \cdot \left(-\sigma_m \nabla \phi_m + 1_{int} \left[i_0 \frac{c_{O_2}}{c_{O_2,ref}} \exp\left(\frac{-\alpha_c F}{RT} \eta \right) \right] \right) = 0. \quad (14)$$

The membrane conductivity is dependent upon the temperature and water vapor concentration. For this simulation, it is assumed that the membrane is recast at 120 °C, and a curve-fit of experimental data [26] is used to compute the membrane conductivity in the ionomer phase as

$$\sigma_m\,(\mathrm{S\,cm^{-1}}) = c_1 \exp([c_2 T - c_3 T^2 + c_4 T^3 - c_5 T^4] a) + c_6. \quad (15)$$

The relative humidity a is computed as

$$a = \frac{c_{H_2O} RT}{P_{sat}}, \quad (16)$$

while the saturation pressure P_{sat} is computed as

$$P_{sat}\,(\mathrm{Pa}) = p_1 + p_2(T - 273) - p_3(T - 273)^2 + p_4(T - 273)^3. \quad (17)$$

The curve-fitting parameters for Eqs. (15) and (17) are given in Table 1.

The electron continuity equation consists of a conduction and a consumption term and is given as

$$\nabla \cdot \left(\sigma_s \nabla \phi_s + 1_{int} \left[i_0 \frac{c_{O_2}}{c_{O_2,ref}} \exp\left(\frac{-\alpha_c F}{RT} \eta \right) \right] \right) = 0. \quad (18)$$

The solid conductivity σ_s is 10 S cm^{-1} [27] in the carbon region and is zero in the pore and ionomer regions.

Table 2
Thermal conductivities for different regions of the catalyst layer.

Region	λ (W cm^{-1} K^{-1})
Pore	2.99
Ionomer	20.0 [28]
Carbon	37.5 [29]

Table 3
Test matrix of boundary conditions.

Parameter	Set 1		Set 2	
	Boundary 1	Boundary 2	Boundary 1	Boundary 2
T (K)	343.0	343.001	353.0	353.001
c_{O_2} (mol m^{-3})	14.1	14.0	7.1	7.0
c_{H_2O} (mol m^{-3})	10.0	10.1	8.0	8.1

The heat equation consists of a conduction term, ohmic heating terms, and reaction heating terms and is given as

$$\nabla \cdot (-\lambda \nabla T) = \frac{(\nabla \phi_s)^2}{\sigma_s} + \frac{(\nabla \phi_m)^2}{\sigma_m} - 1_{int} \nabla \cdot \left[i_0 \frac{c_{O_2}}{c_{O_2,ref}} \exp\left(\frac{-\alpha_c F}{RT} \eta \right) \right] (\eta + \Pi), \quad (19)$$

where λ is the thermal conductivity. The thermal conductivities used in each region are shown in Table 2.

The Peltier coefficient Π for the oxygen reduction reaction can be approximated as [30]

$$\Pi_h \approx T \frac{\Delta S_h}{4F}, \quad (20)$$

where ΔS_h is the entropy change of the half-cell reaction, which is taken to be 326.6 J mol^{-1} K^{-1} [31] for the simulation.

2.3. Boundary conditions

In the three-dimensional domain, Dirichlet boundary conditions are applied at two opposite faces of the cubic domain, while periodic boundary conditions are imposed at the other four faces. A test matrix of simulation cases is considered with a number of varying boundary conditions, which are shown in Table 3. A small temperature difference of 0.001 K between opposite boundaries is imposed, while oxygen and water vapor concentrations differ by 0.1 mol m^{-3} on opposite boundaries. In addition to the boundary conditions listed in Table 3, cases are run on microstructures with sphere radii of 12 nm and microstructures with sphere radii of 20 nm. Thus 16 different sets of simulation data are run using different sphere radii and the different combinations of data considered in Table 3.

The ion and electron potential boundary conditions are the same for every simulation case and are given in Table 4. In the cathode of a PEM fuel cell catalyst layer, the proton and electron current is driven by the consumption of protons and electrons. The electrons have no place to go once they reach the membrane side of the catalyst layer and the protons cannot go anywhere once they reach the GDL side of the catalyst layer. Thus, their potentials were specified such that the proton and electron currents through the random microstructures are approximately equal and the overpotential at each boundary is close to 0.4 V (typical for high current densities).

Table 4
Potential boundary conditions.

Variable	Boundary 1	Boundary 2
ϕ_m	1.7	1.704
ϕ_s	1.3	1.3001

2.4. Numerical method

The governing equations are discretized according to the finite volume method. A Newton–Raphson solver which implements the generalized minimal residual method (GMRES) [32] with a localized Incomplete LU preconditioner [33] is used to solve the discretized governing equations. The simulations are parallelized using the Message Passing Interface (MPI) Library [34] and are run on 16 processors. The simulations are considered to be converged when the nonlinear rms is converged to machine zero. The consistency of the simulation results are verified by comparing the total oxygen consumption, total proton consumption, total electron consumption and total water production values. More details on the numerical approach for a similar problem are given in [35].

The effective transport parameters for the simulation are computed in the following manner. The total flux for any given quantity g (heat or species) can be represented by an effective transport parameter M_{eff}, the length of the solution domain l, and the specified values at opposite boundaries g_1 and g_2. Using this notation, the total flux through the solution domain Λ_g is expressed as

$$\Lambda_g = -M_{eff} \frac{(g_2 - g_1)}{l}. \quad (21)$$

The specified boundary conditions and length of the domain are known. The total flux through the domain Λ_g can be computed from the simulation. Thus, the effective transport parameter can be computed as

$$M_{eff} = -\frac{\Lambda_g l}{(g_2 - g_1)}. \quad (22)$$

The computation of the flux Λ_g is rather straightforward when electrochemical reactions are not considered in the model. In this case, the influx at one boundary must equal to the outflux at the opposite boundary. However, when electrochemical reactions are considered in the model, there is net production or consumption in the domain, and the total influx and outflux values are not equal. In the current work, it was observed that the differences between the influx and outflux values for each species are quite small and thus it is reasonable to use the outflux values when computing the effective transport parameters.

3. Results

Simulations are run for the aforementioned 16 data sets for a wide variety of random microstructures which have pore volume fractions between 25 and 50 percent. For each reconstructed microstructure, simulation results are computed for three orientations. Each orientation has specified dirichlet boundary conditions at different opposing boundaries: one for the x boundaries (on the y–z planes), one for the y boundaries (on the x–z planes) and one for the Z boundaries (on the x–y planes). The consumption values and effective transport parameters computed from these three simulations are averaged. It is the average values that are represented in subsequent plots.

Given that the operating conditions for each case are different, these correspond to different current densities that would be found in a fuel cell. However, only a 200 nm × 200 nm × 200 nm section of the catalyst layer is considered, and thus precise values for fuel cell current densities cannot be obtained. In particular, at low relative humidities, it is likely that the electrochemical reaction will only take place in a very thin layer of the catalyst layer that is close to the membrane. Once all of the incoming protons have been consumed through electrochemical reactions, the remainder of the catalyst layer will be inactive.

However, one can obtain approximate current density ranges for the given cases. In this case, one can convert the total oxygen con-

Table 5
Relative humidity values and approximate current density ranges for considered cases.

T (K)	c_{H_2O} (mol m^{-3})	c_{O_2} (mol m^{-3})	a	Current density (A cm^{-2})
343	10	14	0.91	0.75–1.5
343	10	7	0.91	0.38–0.75
343	8	14	0.73	0.33–0.66
343	8	7	0.73	0.17–0.33
353	10	14	0.62	0.33–0.61
353	10	7	0.62	0.17–0.30
353	8	14	0.49	0.06–0.17
353	8	7	0.49	0.03–0.08

sumption values (mol s^{-1}) into the total reaction current in A cm^{-3}. In order to estimate the current density for a given case, this reaction current can be multiplied by the effective reaction thickness of the catalyst layer. The simulation results indicate that the limiting factor in catalyst layer utilization is the low membrane conductivity, and this can then be used to determine an effective reaction thickness. Thus, for the case with the highest relative humidity value (T = 343 K, c_{H_2O} = 10 mol cm^{-3}), it is assumed that this length is between half the catalyst layer thickness and the entire catalyst layer thickness (taken to be 10 μm here). Thus, an approximate current density range can be obtained for this case. For cases with lower relative humidities, a factor is introduced based on the ratio of the membrane conductivity to the conductivity at the maximum relative humidity.

Based on these calculations, Table 5 lists the approximate range of relative humidities, conversion factors, and approximate range of current densities for each case. Because the membrane conductivity is computed based on experimental data taken for a specific recast membrane, the current densities at low relative humidity values are very small. These values will change when different membranes are used.

3.1. Effective transport parameters

Previous modeling work [13] indicated that when larger carbon spheres are used, larger pores are created between the carbon spheres which results in higher Knudsen diffusivities and hence higher effective oxygen diffusivities. The same phenomenon is observed here, as shown in Fig. 2. There was very little change observed in the effective oxygen diffusivity when the temperature boundary conditions were changed within a normal operating range (343–353 K).

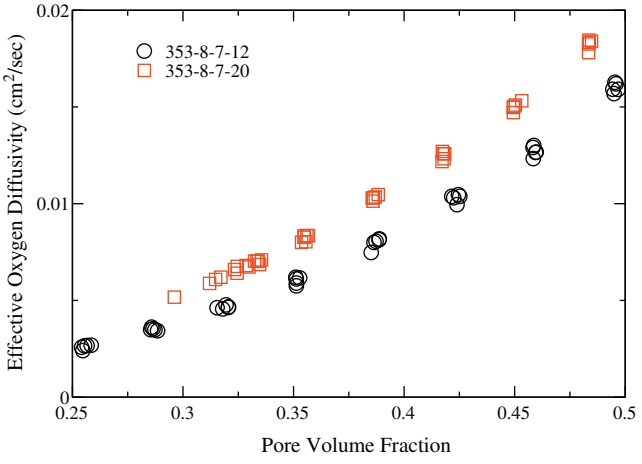

Fig. 2. Effective diffusivities of oxygen for cases with different sphere radii. The four numbers in the series label correspond to T (K), R (mol m^{-3}), P_{sat} (mol m^{-3}), sphere radius (nm).

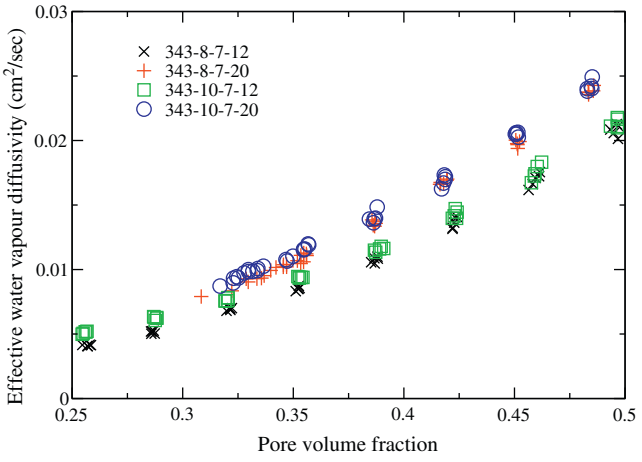

Fig. 3. Effective diffusivities of water vapor for cases with different sphere radii and water vapor concentrations. Labels: T (K), c_{H_2O} (mol m^{-3}), c_{O_2} (mol m^{-3}), sphere radius (nm).

Fig. 3 shows the computed effective water vapor diffusivity for four different sets of data. Similar to the effective oxygen diffusivity data, when larger carbon spheres are used, larger effective diffusivities are obtained due to larger pores and higher Knudsen numbers. Another interesting feature of the data is that at low pore volume fractions, data sets with higher water vapor concentrations have higher effective diffusivities. This is due to the phenomenon of electro-osmotic drag. Since the potential difference across the catalyst layer sample is prescribed, at higher water vapor concentrations, there is increased proton transport through the membrane due to higher membrane conductivities. Water vapor molecules attach to the protons and are carried in this manner. This effect is most pronounced at low pore volume fractions, because the ionomer volume fraction is higher and higher effective proton conductivity values are obtained.

Effective proton conductivity data for a wide range of cases is shown in Fig. 4. As expected, the most important factor in determining the effective proton conductivity is the relative humidity, which depends on the temperature and the water vapor concentration as shown in Eq. (16). When larger spheres are used, for a given pore volume fraction, the carbon volume fraction is higher and the ionomer volume fraction is lower, hence the data for the larger spheres corresponds to lower ionomer volume fraction values. The effective electron conductivity data is shown in Fig. 5. The

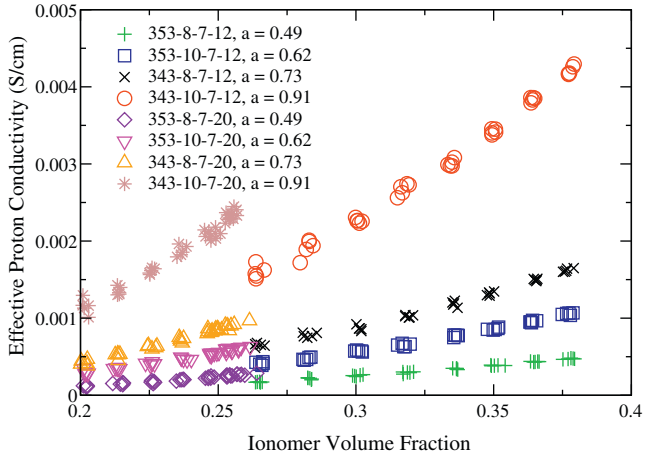

Fig. 4. Effective proton conductivities for cases with different sphere radii, water vapor concentrations, and temperatures. Labels: T (K), c_{H_2O} (mol m^{-3}), c_{O_2} (mol m^{-3}), sphere radius (nm), relative humidity.

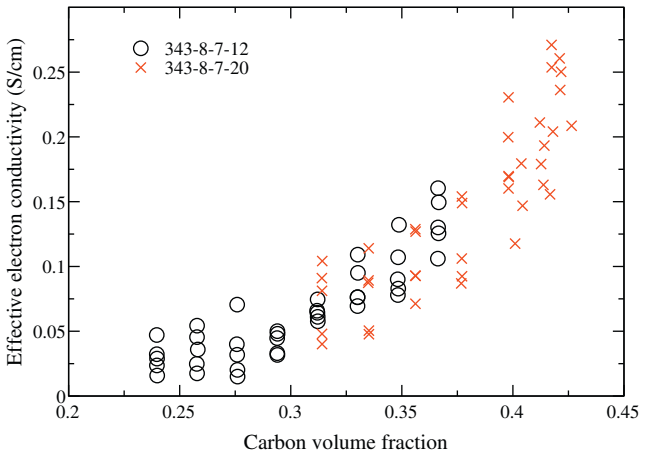

Fig. 5. Effective electron conductivities for cases with different sphere radii. Labels: T (K), c_{H_2O} (mol m^{-3}), c_{O_2} (mol m^{-3}), sphere radius (nm).

effective electron conductivities are much larger than the effective proton conductivities, because the bulk electron conductivity is much larger. There is also much more variance in the effective electron conductivity data. This may be due to the low overlap tolerance and the presence of isolated, disconnected carbon spheres that are present in some microstructures.

Figs. 6 and 7 show the effective thermal conductivity as a function of pore volume fraction and ionomer volume fraction, respectively. As the porosity of the catalyst layer is increased, the thermal conductivity decreases, because the thermal conductivity of air is the lowest of the three phases. The amount of ionomer in the catalyst layer increases with the number of carbon spheres, and thus the thermal conductivity increases with an increase in the ionomer volume fraction.

3.2. Consumption plots

Figs. 8 and 9 show the total oxygen consumption in the catalyst layer sample for cases run at 343 and 353 K. It is clear from the data that at higher oxygen concentrations and higher temperatures, higher consumption values are obtained. This is consistent with the Tafel equation and the expressions for exchange current density and the charge transfer coefficient as given in Eqs. (6) and (7). Another dominant trend is that as the pore volume fraction increases, the total consumption decreases. This is due

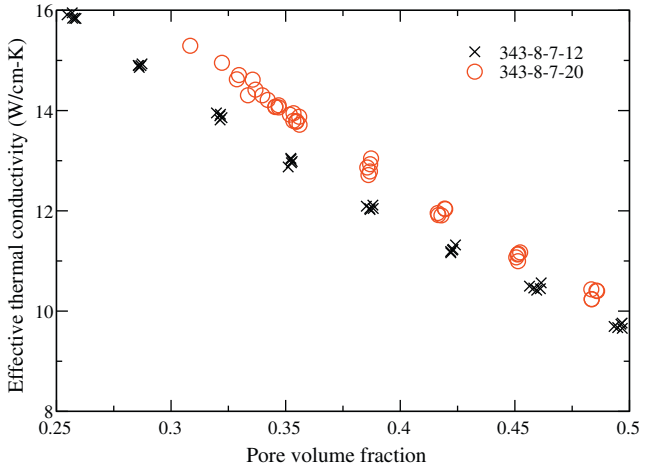

Fig. 6. Effective thermal conductivities as a function of pore volume fraction. Labels: T (K), c_{H_2O} (mol m^{-3}), c_{O_2} (mol m^{-3}), sphere radius (nm).

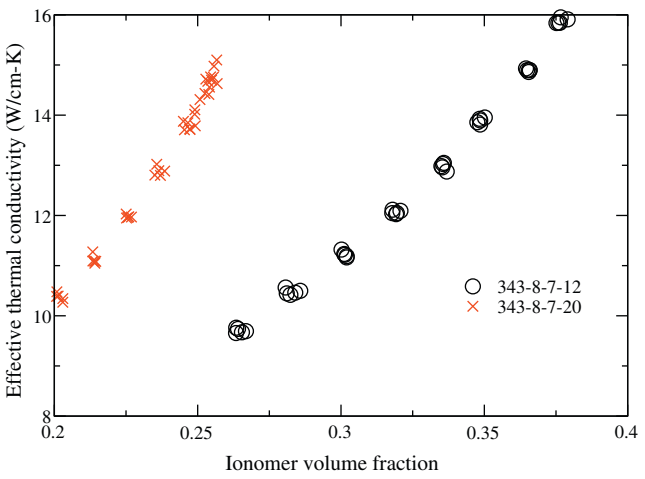

Fig. 7. Effective thermal conductivities as a function of ionomer volume fraction. Labels: T (K), c_{H_2O} (mol m^{-3}), c_{O_2} (mol m^{-3}), sphere radius (nm).

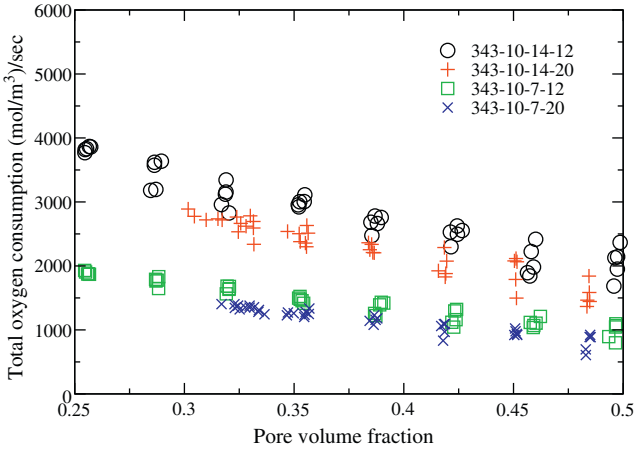

Fig. 8. Total oxygen consumption as a function of pore volume fraction at 343 K. Labels: T (K), c_{H_2O} (mol m^{-3}), c_{O_2} (mol m^{-3}), sphere radius (nm).

to the fact that there are more carbon spheres in the microstructures at low pore volume fractions and thus more area available for electrochemical reactions. When larger carbon spheres are used, there is less surface area for reactions at a given carbon volume fraction than when smaller carbon spheres are used. Thus, lower

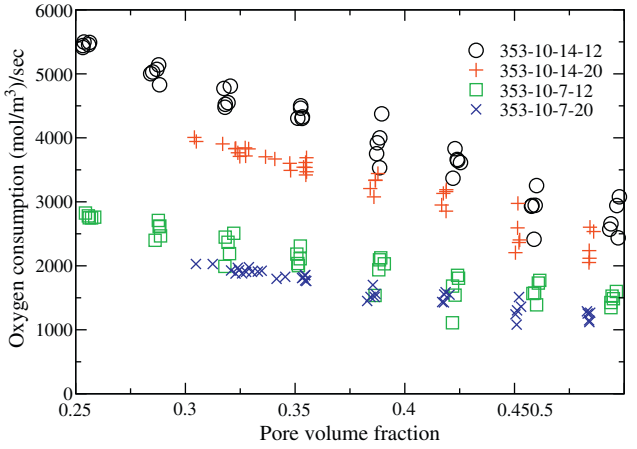

Fig. 9. Total oxygen consumption as a function of pore volume fraction at 353 K. Labels: T (K), c_{H_2O} (mol m^{-3}), c_{O_2} (mol m^{-3}), sphere radius (nm).

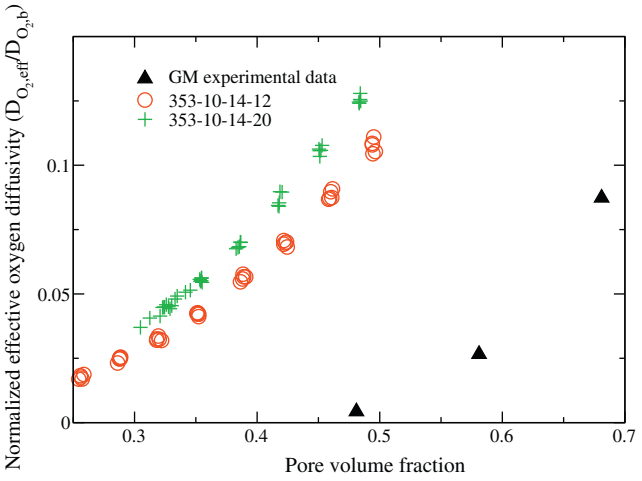

Fig. 10. Comparison of simulation data with experimental data [36] for effective oxygen diffusivity.

consumption values are obtained when larger carbon spheres are used.

4. Discussion

Comparing the results obtained from the computational model with published experimental data yields further insights. Recently, the effective oxygen diffusivity through a PEM fuel cell catalyst layer was measured by researchers from General Motors Corporation [36] at a temperature of 353 K and a pressure of 1 atm. Their values are much lower than those found in the simulations, as shown in Fig. 10.

The trends are similar, but it appears that the effective diffusivity curves found from the simulations are shifted to the left relative to the experimental data. A number of reasons could account for this shift. Liquid water is not accounted for in the model and this may present an impediment to oxygen diffusion. Also, ionomer swelling is not taken into account in the model. The swelling of the ionomer film could constrict the pores, resulting in lower pore diameters and thus lower effective diffusivities. However, it is unlikely that these aspects can alone explain the difference in the results, because the experimental results show only a small change in the measured effective diffusivities when the relative humidity is changed from 0 to 100 percent.

An alternative explanation for the discrepancy is that the assumption of a uniformly thin ionomer film is not valid. A uniformly thin layer around the carbon spheres does not present a significant resistance to oxygen diffusion through the catalyst layer, since the oxygen already has to travel around the carbon spheres. Some self-organization studies have predicted that the surface of the carbon particles is not completely covered by the ionomer [37]. If the ionomer is distributed nonuniformly, this might present more of a barrier for oxygen diffusion as ionomer filaments and agglomerates may protrude into pores between the carbon spheres. An example of this is shown in Fig. 11. The nonuniform ionomer distribution would significantly change the pore morphology, increase the tortuosity of diffusing gases and decrease their effective diffusivities. Verification of this conjecture has to await progress in detailed characterization of the catalyst layer morphology.

An additional assumption of the model is that the ionomer distribution and porosity throughout the length of the catalyst layer are approximately uniform. This assumption allows computation of the effective transport properties from a computational domain with dimensions that are 2 orders of magnitude smaller than the thickness of most catalyst layers. If, however, there was more ionomer distributed towards one end of the catalyst layer than the other (meaning that the porosity through the catalyst layer also varies), this would represent a significant barrier for oxygen transport. The measured effective oxygen diffusivity throughout the entire catalyst layer would be much lower for a catalyst layer with inhomogeneous porosities and ionomer distributions.

Finally, the Knudsen diffusivity is derived for one-dimensional transport in a straight channel. Every molecule that collides with the wall changes its direction but continues to move towards regions of lower concentrations. In the case of a PEM fuel cell catalyst layer, the microstructure is composed of randomly placed carbon spheres. Molecular collisions may redirect molecules towards regions of higher concentrations and this effect would significantly reduce the effective diffusivity. Furthermore, oxygen molecules in the catalyst layer "collide" with an ionomer layer which is permeable to oxygen. This is different from classical Knudsen diffusion where molecules collide with impermeable structures.

An interesting insight from these results comes from the fact that agglomerates are not explicitly formed in the reconstruction process. Each carbon sphere is placed individually in the domain, resulting in a unimodal pore size distribution. An alternative approach would be to form agglomerates with a specified number of carbon spheres, and form the catalyst layer microstructure by placing agglomerates in the domain, covering the agglomerates with ionomer. This would create a bimodal pore size distribution in the domain due to micropores inside the agglomerates and macropores between the agglomerates. However, if such a scheme were

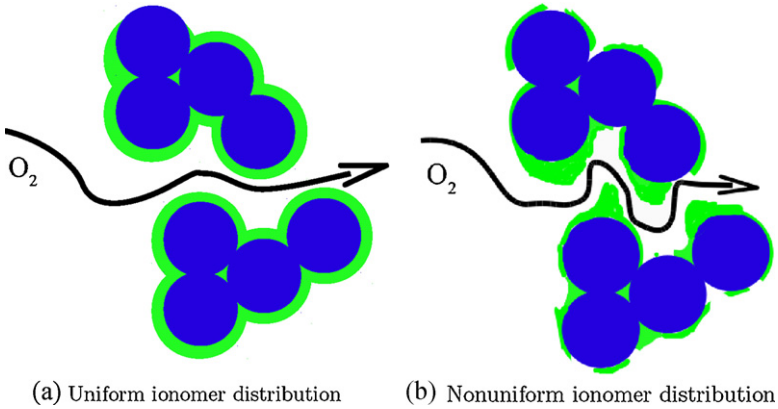

Fig. 11. Schematic showing diffusion paths for oxygen in microstructures with different ionomer distributions. It is clear that the oxygen in Fig. 11b has a more tortuous path to travel.

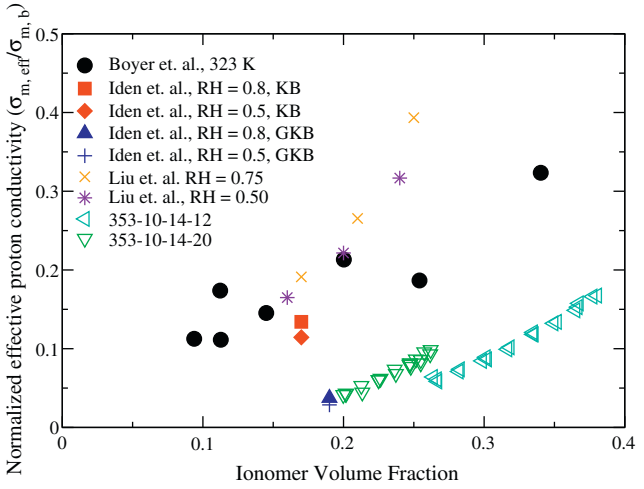

Fig. 12. Comparison of simulation data with experimental data for the effective proton conductivity of the catalyst layer. Measurements are assumed to take place at 353 K unless otherwise specified. The data by Iden et al. was taken for two pseudo catalyst layers: one with Ketjen Black (KB) as the carbon support and one with graphitized Ketjen Black (GKB) as the carbon support.

implemented in the current model, the effective diffusivities of oxygen would be higher due to the presence of macropores, which would reduce the impact of Knudsen diffusion. Thus, for a model which considered agglomerates, there would be an even larger difference between experimental and computational results.

A number of experimental works have sought to measure the effective proton conductivity or resistance through the catalyst layer of a PEM fuel cell [38–42]. In general, the experimental data has shown a linear relationship between the effective proton conductivity and the ionomer volume fraction [38,41], which is qualitatively similar to the computational results, as shown in Fig. 12. However, the normalized effective conductivity values computed by the simulations for a given ionomer volume fraction are much lower than values obtained from experiments, with the exception of the data taken from the catalyst with graphitized Ketjen Black (GKB).

The discrepancy between experimental and computational results again calls into question the aforementioned assumption of uniformly thin ionomer layers. This assumption requires the protons to travel close to the surface of the carbon spheres and the tortuosity may be decreased if there are more direct routes that protons can take. These may be created by having thicker ionomer regions at the intersections between two carbon spheres. Another consideration is that the current model uses an approximately constant ionomer/carbon (I/C) ratio for a given carbon sphere radius and ionomer thickness regardless of the porosity (1.1 for carbon sphere radii of 12 nm and 0.7 for carbon sphere radii of 20 nm with ionomer thicknesses of 4 nm). The model also assumes that the carbon spheres all have the same radii. It is more likely that there is a distribution with regard to the size of the carbon particles, and in a previous work, it was observed that the ionomer conductivity increased when a normal distribution of carbon particles was used [13].

However, the fact that the experimental data yields tortuosity factors that are less than or close to one indicates that there must be a different mechanism of proton transport in thin ionomer films on carbon than what is measured with bulk conductivity values. Tortuosity values of less than one are unphysical. It is also highly unlikely that the actual tortuosity is close to one because this implies that there are straight proton-conducting ionomer "tubes" which span the entire thickness of the catalyst layer from one side to the other.

There are several possibilities as to what this different mechanism might be, with interactions between the carbon support material and the ionomer being one possibility. The proton conductivity of the ionomer has been shown to depend on the carbon material [42] and on the I/C ratio [41]. Indeed, results from the computational model are very close to experimental data obtained using GKB as a carbon support [42]. An additional possibility is that some mechanism of surface diffusion takes place as there is a much higher surface to volume ration for thin ionomer films than for bulk films. Finally, some have suggested that proton transport in the catalyst layer occurs through water [37] and this additional transport mechanism may serve to increase the total effective proton conductivity through the catalyst layer.

The insights that have been obtained from comparing the results of this model with experimental results can be used to guide the future development of catalyst layer models and raise a number of questions. Research must be done to obtain an expression for the Knudsen diffusivity which is more appropriate for catalyst layer microstructures. In addition, different reconstruction methods must be investigated to determine the effect of the ionomer distribution on the effective oxygen diffusivity. To improve the model of proton transport, experimental proton conductivity values should be obtained for thin ionomer films on carbon supports instead of bulk ionomer membranes.

Future development of the catalyst layer model will incorporate the discrete placement of platinum particles and a correlation with the platinum loading, ionomer swelling, and the presence of liquid water. In addition, the model will account for multispecies diffusion and for variations in the thermal conductivity of the ionomer due to changes in the temperature and relative humidity.

5. Conclusions

A fully coupled model has been developed for the simulation of oxygen, protons, electrons, water vapor and temperature in a small section of the catalyst layer of a PEM fuel cell. Effective transport parameters and consumption values are computed for a large range of different microstructures for a wide variety of operating conditions. The differences between the simulation results and published experimental results are discussed and the model assumptions are critically re-examined to provide insight and guidance for the development of accurate catalyst layer simulations.

Acknowledgments

This work was funded through the Natural Science and Engineering Research Council (NSERC) Discovery Grant program and the Canada Research Chairs Program.

References

[1] M. Secanell, R. Songprakorp, A. Suleman, N. Djilali, Energy Environ. 1 (2008) 378–388.
[2] Y. Shao, G. Yin, Y. Gao, J. Power Sources 171 (2007) 558–566.
[3] A. Kusoglu, Y. Tang, M. Lugo, A.M. Karlsson, M.H. Santare, S. Cleghorn, W.B. Johnson, J. Power Sources 195 (2010) 483–492.
[4] S. Litster, N. Djilali, Electrochim. Acta 52 (2007) 3849–3862.
[5] G. Wang, Ph.D. thesis, The Pennsylvania State University (2003).
[6] G. Wang, P.P. Mukherjee, C.-Y. Wang, Electrochim. Acta 51 (2006) 3139–3150.
[7] G. Wang, P.P. Mukherjee, C.-Y. Wang, Electrochim. Acta 51 (2006) 3151–3160.
[8] P.P. Mukherjee, C.-Y. Wang, J. Electrochem. Soc. 153 (2006) A840–A849.
[9] G. Wang, P.P. Mukherjee, C.-Y. Wang, Electrochim. Acta 52 (2007) 6367–6377.
[10] M. Secanell, K. Karan, A. Suleman, N. Djilali, Electrochim. Acta 52 (2007) 6318–6337.
[11] S.H. Kim, H. Pitsch, J. Electrochem. Soc. 156 (2009) B673–B681.
[12] N. Siddique, F. Liu, Electrochimica Acta 55 (2010) 5357–5366.
[13] K.J. Lange, P.-C. Sui, N. Djilali, J. Electrochem. Soc. 157 (2010) B1434–B1442.
[14] T. Hattori, A. Suzuki, R. Sahnoun, M. Koyama, H. Tsuboi, N. Hatakeyama, A. Endou, H. Takaba, M. Kubo, C.A.D. Carpio, A. Miyamoto, Appl. Surf. Sci. 254 (2008) 7929–7932.

[15] E.A. Mason, A.P. Malinauskas, R. B. E. III, J. Chem. Phys. 46 (1967) 3199–3216.
[16] E. Mason, A. Malinauskas, Gaseous transport in porous media: the dusty-gas model, Elsevier, Amsterdam (1983).
[17] D. Bruggeman, Ann. Phys. 24 (1935) 636–664.
[18] R. Cunningham, R. Williams, Diffusion in Gases and Porous Media, Plenum, New York (1980).
[19] M. Mench, Fuel Cell Engines, John Wiley & Sons, Hoboken, New Jersey, 2008.
[20] E. Cussler, Diffusion: Mass Transfer in Fluid Systems, Cambridge University Press, 1997.
[21] W.G. Pollard, R.D. Present, Phys. Rev. 73 (1948) 762–774.
[22] K. Lee, A. Ishihara, S. Mitsushima, N. Kamiya, K. ichiro Ota, J. Electrochem. Soc. 151 (2004) A639–A645.
[23] A. Parthasarathy, S. Srinivasan, A.J. Appleby, C.R. Martin, J. Electrochem. Soc. 139 (1992) 2530–2537.
[24] S. Motupally, A.J. Becker, J.W. Weidner, J. Electrochem. Soc. 147 (2000) 3171–3177.
[25] T.A. Zawodzinski, J. Davey, J. Valerio, S. Gottesfeld, Electrochim. Acta 40 (1995) 297–302, polymer electrolyte fuel cells.
[26] Y. Sone, P. Ekdunge, D. Simonsson, J. Electrochem. Soc. 143 (1996) 1254–1259.
[27] N. Probst, E. Grivei, Carbon 40 (2002) 201–205.
[28] M. Khandelwal, M. Mench, J. Power Sources 161 (2006) 1106–1115.
[29] J.-B. Donnet, R.C. Bansal, M.-J. Wang, Carbon black: science and technology, Marcel Dekker, Inc., New York, NY, USA, 1993.
[30] A.Z. Weber, J. Newman, J. Electrochem. Soc. 153 (2006) A2205–A2214.
[31] M.J. Lampinen, M. Fomino, J. Electrochem. Soc. 140 (1993) 3537–3546.
[32] Y. Saad, M.H. Schultz, SIAM J. Sci. Stat. Comput. 7 (1986) 856–869.
[33] K. Nakajima, H. Okuda, Int. J. Comput. Fluid Dyn. 12 (1999) 315–322.
[34] A. Grama, A. Gupta, G. Karypis, V. Kumar, Introduction to Parallel Computing, Addison-Wesley, 2003.
[35] K. Lange, C. Misra, P.-C. Sui, N. Djilali, accepted for publication in Comput, Methods Appl. Mech. Engrg. (2010).
[36] Z. Yu, R.N. Carter, J. Power Sources 195 (2010) 1079–1084.
[37] K. Malek, M. Eikerling, Q. Wang, T. Navessin, Z. Liu, J. Phys. Chem. C 111 (2007) 13627–13634.
[38] C. Boyer, S. Gamburzev, O. Velev, S. Srinivasan, A.J. Appleby, Electrochim. Acta 43 (1998) 3703–3709.
[39] G. Li, P.G. Pickup, J. Electrochem. Soc. 150 (2003) C745–C752.
[40] C.Y. Du, P.F. Shi, X.Q. Cheng, G.P. Yin, Electrochem. Commun. 6 (2004) 435–440.
[41] Y. Liu, M.W. Murphy, D.R. Baker, W. Gu, C. Ji, J. Jorne, H.A. Gasteiger, J. Electrochem. Soc. 156 (2009) B970–B980.
[42] H. Iden, A. Ohma, K. Shinohara, J. Electrochem. Soc. 156 (2009) B1078–B1084.

Glossary

1_{int}: term is equal to one at carbon/ionomer interface and zero elsewhere
a: relative humidity
c_1: coefficient for membrane conductivity ($S\,cm^{-1}$)
c_2: coefficient for membrane conductivity (K^{-1})
c_3: coefficient for membrane conductivity (K^{-2})
c_4: coefficient for membrane conductivity (K^{-3})
c_5: coefficient for membrane conductivity (K^{-4})
c_6: coefficient for membrane conductivity ($S\,cm^{-1}$)
c_{H_2O}: water vapor concentration ($mol\,cm^{-3}$)
c_{O_2}: oxygen concentration ($mol\,cm^{-3}$)
$c_{O_2,ref}$:: reference oxygen concentration ($mol\,cm^{-3}$)
d_p: pore diameter (cm)
D_{H_2O}: water vapor diffusivity ($cm^2\,s^{-1}$)
$D_{H_2O,b}$: bulk water vapor diffusivity in pore region ($cm^2\,s^{-1}$)
$D_{H_2O,i}$: ionomer water vapor diffusivity ($cm^2\,s^{-1}$)
$D_{H_2O,Kn}$: Knudsen water vapor diffusivity in pore region ($cm^2\,s^{-1}$)
D_{O_2}: oxygen diffusivity ($cm^2\,s^{-1}$)
$D_{O_2,b}$: bulk oxygen diffusivity in pore region ($cm^2\,s^{-1}$)
$D_{O_2,i}$: ionomer oxygen diffusivity ($cm^2\,s^{-1}$)
$D_{O_2,Kn}$: Knudsen oxygen diffusivity in pore region ($cm^2\,s^{-1}$)
F: Faraday's constant ($C\,mol^{-1}$)
g: solution variable for quantity in the domain
g_1: solution variable at boundary 1
g_2: solution variable at boundary 2
i_0: exchange current density ($A\,cm^{-2}$)
l: length of the solution domain (cm)
M_{eff}: effective transport parameter
n_d: electro-osmotic drag coefficient
p: pressure (atm)
p_1: coefficient for saturation pressure (Pa)
p_2: coefficient for saturation pressure ($Pa\,K^{-1}$)
p_3: coefficient for saturation pressure ($Pa\,K^{-1}$)
p_4: coefficient for saturation pressure ($Pa\,K^{-1}$)
P_{sat}: saturation pressure (Pa)
R: universal gas constant ($J\,mol^{-1}\,K^{-1}$)
ΔS_h: change in entropy ($J\,mol^{-1}\,K^{-1}$)
T: temperature (K)

Greek symbols

α_c: charge transfer coefficient
η: overpotential (V)
λ: thermal conductivity ($W\,cm^{-1}\,K^{-1}$)
Λ_g: total flux through the domain
Π: Peltier coefficient ($J\,C^{-1}$)
σ_m: membrane conductivity ($S\,cm^{-1}$)
σ_s: solid conductivity ($S\,cm^{-1}$)
ϕ_m: membrane potential (V)
ϕ_s: solid potential (V)